5th Joint International Symposium on Deformation Monitoring (JISDM), 20-22 June 2022, Valencia, Spain
DOI: http://doi.org/10.4995/JISDM2022.2022.13812

# Keypoint-based deformation monitoring using a terrestrial laser scanner from a single station: Case study of a bridge pier

Tomislav Medic[1], Pia Ruttner[1], Christoph Holst[2], Andreas Wieser[1]

[1] Institute of Geodesy and Photogrammetry, ETH Zürich, Stefano-Franscini-Platz 5, 8093 Zurich, Switzerland, (tomislav.medic@geod.baug.ethz.ch; pia.ruttner@geod.baug.ethz.ch; andreas.wieser@geod.baug.ethz.ch)
[2] TU Munich, TUM School of Engineering and Design, Chair of Engineering Geodesy, 80333 Munich, Germany, (christoph.holst@tum.de)

**Key words**: *deformation monitoring*; *LiDAR*; *point clouds*; *change detection*; *time series; intensity image features*

**ABSTRACT**

Terrestrial laser scanners (TLSs) offer a possibility for more automated and efficient deformation monitoring of civil engineering structures with higher spatial resolution than standard methods, as well as without the necessity of permanently installing the monitoring equipment. In such applications, scanners are usually placed so that the lines of sight are roughly aligned with the main directions of the expected deformations, and the deformations are estimated from point cloud differences between multiple epochs. This allows high sensitivity in the direction of the surface normal, but deformations along the surface are often undetected or hard to precisely quantify. In this work, we propose an algorithm based on the detection and matching of keypoints identified within TLS intensity images. This enables precise quantification of deformations along the scanned surfaces. We also present the application of the algorithm for monitoring a bridge pier of the Hochmoselbrücke in Germany, as a case study. Deformations up to about 4 cm due to thermal expansion and bending of the pier were successfully detected from scans taken throughout the day from a single location, up to 180 m from the monitored surfaces. The results agreed within a few millimeters to independent monitoring using state-of-the-art processing of TLS point clouds obtained from a different location and using a different type/brand of instrument. The newly proposed algorithm can either be used to complement existing TLS-based deformation analysis methods by adding sensitivity in certain directions, or it can be valuable as a standalone solution.

## I. INTRODUCTION

Terrestrial laser scanners (TLSs) are increasingly used for deformation monitoring of structures and landmasses (Mukupa *et al.,* 2017). The deformations are characterized as differences between point clouds represented in a common coordinate system. These differences are often defined as Euclidean distances between nearest neighbors in certain directions, *e.g.*, along the local surface normals. Commonly used algorithms are the cloud-to-cloud (C2C), cloud-to-mesh (C2M), and Multiscale Model-to-Model Cloud Comparison (M3C2) algorithm (Lague *et al.,* 2013), see e.g. (Holst *et al.,* 2017). Comparable alternatives are using patch-wise ICP (Iterative Closest Point) to estimate 3d displacement vectors (Friedli and Wieser 2016; Wujanz *et al.,* 2016) and parametric modeling of point cloud surfaces, where deformations are represented by parameter changes (Neuner *et al.,* 2016). Most of these methods are relatively insensitive (*i.e.* "blind") to deformations occurring along the surface of the observed object.

A few algorithms were proposed to overcome these limitations (Gojcic *et al.,* 2020; 2021; Holst *et al.,* 2021). They substitute comparing nearest neighbors in Euclidian space by searching the corresponding points in a high-dimensional feature space. Feature description algorithms are used to encode the geometry or structure of the neighborhood of the individual points in the point clouds. This allows finding the correct point correspondences, even if the deformations occurred along the surface of the observed object. The latter algorithms were successfully used in geomonitoring, where the irregular structure of landmasses provided a sufficient amount of details for unambiguous point description and matching. However, these algorithms cannot resolve the problem of detecting deformations along surfaces that lack (sufficiently pronounced and unique) geometric features which would characterize the neighborhood of the individual points unambiguously. This limits their use for structural monitoring where the surfaces are often smooth or composed of repetitive structure.

This problem can be solved by placing artificial laser-scanning targets at the surfaces. However, this will often be labor intensive –if not impossible (*e.g.*, with surfaces out of reach)–, and additionally questions the application of a scanner in the first place. Nevertheless, scanning targets often feature specific radiometric patterns and are used by processing the intensity data provided by the scanner rather than just the geometry.

Picking up this idea, we propose herein to substitute feature descriptors based on the geometric surface structure with a descriptor based on the intensity values of the returned laser beams. Although this could be combined with geometric features for monitoring, we will investigate the intensity-based approach on its own, herein. Instead of trying to find correspondences for all points in the point cloud (as in, *e.g.* Gojcic *et al.,* 2021), we adopt the approach of considering only keypoints, *i.e.* points that can be well located in the scan and whose neighborhood can be unambiguously described. The corresponding points are found automatically in the scene using the existing feature description and matching algorithms for 2D local image keypoints (Jing *et al.*, 2021). To achieve this, we exploit the regular and nearly continuous TLS scanning pattern to map the 3D TLS measurements onto 2D intensity images. To find multiple keypoint correspondences with sufficient localization accuracy for deformation monitoring, it is necessary to avoid strong changes in the measurement configuration, as they cause image distortions and changes in the intensity values. Hence, we limited our approach to deformation monitoring from a single scanner station herein and leave generalization for future work.

Similar approaches were used for the registration of TLS point clouds (Urban and Weinmann, 2015) and TLS calibration (Medić *et al.,* 2019). Moreover, a comparable approach was already described for deformation monitoring with scanning total stations, where feature description is based on RGB images taken by the internal camera (Wagner *et al.,* 2017). The approach proposed in this work deviates from the latter one, as it relies only on active sensing with an electronic distance measurement (EDM) unit. This offers some advantages such as insensitivity to ambient illumination allowing operations in changing visibility conditions, during the night and observing the objects that are partially in bright sunlight and partially in shadows.

We tested the algorithm on a particular case study of monitoring a bridge pier deformation from a single scanner station over several hours. In this paper, we compare the results to deformations estimated using the established M3C2 algorithm using point clouds acquired with another TLS from a different location. The presented results are an outcome of the initial analysis and the process is still a work in progress.

## II. Implemented Algorithm

The inputs of the implemented algorithm[1] are registered point clouds, acquired at several epochs from a single scanner station. They refer to a common Cartesian Coordinate system and contain intensity information for each point. To use image processing algorithms for keypoint detection, description and matching, the 3D TLS point cloud data needs to be mapped onto an intensity and range image.

We use the approach described in Medić *et al.* (2019), which relies on spherical image representation. Therein, the point cloud Cartesian coordinates are transformed into spherical ones (range, horizontal and vertical angle). Then, the spherical intensity and range images are generated by linearly interpolating the scanner measurements with a regular spacing, so that the pixel coordinates correspond to the scanner's horizontal and vertical angles and the pixel values correspond to the intensity and range measurements. The image resolution is made equal to the scanning resolutions (angular step sizes) to avoid information loss. It should be noted that such spherical representation has a disadvantage of strong image distortions at high elevation angles. However, such high elevation angles are rarely observed in deformation monitoring, making the approach largely applicable.

Within the spherical intensity images, the keypoints are automatically detected using the Speeded Up Robust Features (SURF) algorithm (Bay *et al.,* 2008) and described using the Binary Robust Invariant Scalable Keypoints (BRISK) algorithm (Leutenegger *et al.,* 2011). The choice is made based on our simplified analysis of different feature detectors and descriptors (Jing *et al.*, 2021), where the selected algorithms outperformed the rest (the differences were in some cases marginal).

The correspondences are searched in 64-dimensional feature space between the first point cloud in the series (epoch 0) and all following $n$ point clouds (epochs $i$, where $i = 1,2, \dots, n$). The points with the minimum Euclidean distance (highest similarity) in the feature space are matched together. We use the prior knowledge that the expected deformations are small (several centimeters), and, therefore, that the corresponding keypoints should be close in space. Hence, only keypoints within a pre-defined neighborhood are considered. The extent of the neighborhood is defined with a spherical distance, corresponding to the pixel-wise distance in the spherical intensity image. We chose this over Euclidean distance in 3D space to avoid using interpolated range values, which could be erroneous when the keypoints are defined on corners and edges. The neighborhood extent is defined by a task-specific user-defined threshold (in this case study 0.05° based on an educated guess).

The keypoint detection returns the keypoint positions as pixel-wise 2D image coordinates. These coordinates are transformed into 3D spherical coordinates by linear interpolation based on the known direct correspondences between row vs. vertical and column vs. horizontal angle, and by directly interpolating ranges from spherical range images (see Medić *et al.*, 2019). Finally, we transform the spherical to Cartesian

[1] Source-code available at https://github.com/ruttnerp/ikptlsdm

coordinates and estimate deformation vectors $\boldsymbol{v}_i^j$ for each pair of matched keypoints as (Eq. 1):

$$\boldsymbol{v}_i^j = [\Delta X, \Delta Y, \Delta Z]_i^j = \boldsymbol{k}_i^j(X,Y,Z) - \boldsymbol{k}_0^j(X,Y,Z) \qquad (1)$$

where $\boldsymbol{k}_i^j(X,Y,Z)$ are the coordinates of a keypoint $j$ ($j = 1,2,\dots,w; w - nr.of\ matched\ keypoints$) in epoch $i$, and $[\Delta X, \Delta Y, \Delta Z]_i^j$ are the corresponding coordinate differences relative to the position of the keypoint $j$ at epoch 0 ($\boldsymbol{k}_0^j$).

As the implemented keypoint matching strategy can still cause incorrect matches (Szeliski, 2022), we implemented an outlier removal strategy based on the local rigidity presumption. We presume that all keypoint coordinate differences within a predefined neighborhood should be similar. For this particular case study, the point cloud of the bridge pier is separated vertically into 5° segments over the spherical intensity images, resulting in overall 10 segments. The segment extent is based on the educated guess with the goal of assuring a sufficient number of matches for the outlier removal. The outliers are determined using the 2 times median absolute deviation from the median (MAD) threshold, multiplied by the scaling factor of 1.4826. The outliers are searched for the following quantities: 2D image coordinate differences, 3D coordinate differences (for each Cartesian and spherical coordinate), 3D vector magnitude and direction (cosine between individual vector to median vector). An example of the output within our case study is presented in Figure 1 (right).

Following the outlier removal step, we refine deformation estimates by averaging all deformation vectors $\boldsymbol{v}_i^j$ for each segment and for each epoch separately (Eq. 2):

$$\overline{\boldsymbol{v}}_i^s = [\overline{\Delta X}, \overline{\Delta Y}, \overline{\Delta Z}]_i^s = \left[\frac{\sum(\Delta X_i^j)^s}{w_i^s}, \frac{\sum(\Delta Y_i^j)^s}{w_i^s}, \frac{\sum(\Delta Z_i^j)^s}{w_i^s}\right] \qquad (2)$$

where $\overline{\boldsymbol{v}}_i^s$ is mean deformation vector of segment $s$ in epoch $i$; $()^s$ denotes a subset of keypoint coordinate differences of epoch $i$ falling within segment $s$ ($s = 1,2,\dots,m; m - nr.of\ segments$); $w_i^s$ is a number of matched keypoints in segment $s$ at epoch $i$. We set a user-defined threshold for a minimum number of keypoint matches per segment for computing $\overline{\boldsymbol{v}}_i^s$ (default value 10 based on initial testing). If the threshold is not reached, we assume that the number of keypoint matches is inadequate for estimating $\overline{\boldsymbol{v}}_i^s$ with sufficient precision. Hence, for such segments $\overline{\boldsymbol{v}}_i^s$ is not defined.

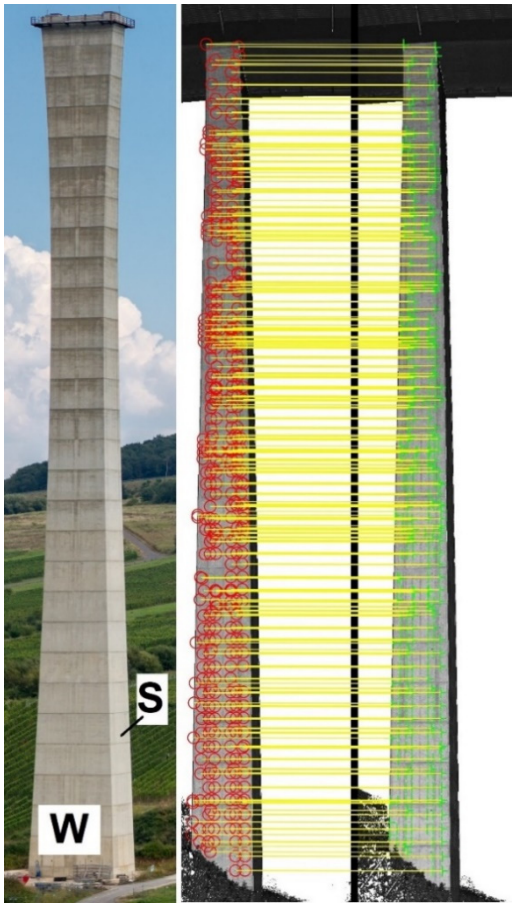


Figure 1. Left - Monitored bridge pier (≈ 140 x 15 x 7 m), Image source: wikipedia.org; Right – Intensity images with keypoints distribution along the "S" side of the bridge pier after matching and outlier removal (red points - epoch 0, green points epoch i, yellow lines – correct matches).

To further improve the quality of deformation estimates, we introduced an additional step of functionally approximating deformations based on case-specific prior knowledge. For our task, the deformation magnitudes smoothly change along the surface of the measured object (highest at the top, zero at base), and with time (zero at epoch 0, maximal at epoch n). The implemented functional approximation of the deformations rests upon the assumption that each pier segment is translated and not deformed over time, while the pier as a whole is deformed due to different translation magnitudes for different segments. The approximation is realized as a robustified best-fit algorithm (least absolute residual - LAR), with a 3rd degree polynomial for a function model (Eq. 3):

$$\begin{aligned} d_i^s(t_i, z_s) = {} & c_{00} + c_{10}\, t_i + c_{01}\, z_s + c_{11}\, t_i\, z_s \\ & + c_{20} {t_i}^2 + c_{02}\, {z_s}^2 \\ & + c_{21} t {t_i}^2 z_s + c_{12} t_i {z_s}^2 \\ & + c_{30}\, {t_i}^3 + c_{03}\, {z_s}^3 \end{aligned} \qquad (3)$$

where $d_i^s(t_i, z_s)$ are the deformation magnitudes (observations) per pier segment $s$ and per epoch $i$, $t_i$ – time of the epoch $i$ (given values), $z_s$ - mean height of the pier segment $s$ (given values), $c_{xx}$ - polynomial

coefficients (estimated parameters). The weight matrix is realized as a unit matrix. The deformation magnitudes $d_i^s$ are calculated as norms of mean deformation vectors per segment (Eq. 4):

$$d_i^s = \|\overline{\boldsymbol{v}}_i^s\| = \|[\overline{\Delta X}, \overline{\Delta Y}, \overline{\Delta Z}]_i^s\| \quad (4)$$

The final output of the algorithm are estimated deformation magnitudes as a function of time and height along the pier. Such deformation representation reduces the amount of information to only the most relevant dimension (deformation magnitude). However, the keypoint-based deformation monitoring allows for generating 3D vector fields, which can also reveal the direction of deformations, de-compose the magnitude along different directions (*e.g.*, horizontally and vertically along the scanned surface or perpendicular to the surface) and uncover eventual inhomogeneities in the object's behavior. However, such interpretation is out of the scope of this work.

## III. Experiment

The implemented algorithm was tested in a case study of monitoring pier deformations of the Hochmosel-bridge in western Germany. The bridge was opened in 2019, is 1700 m long and is supported by ten reinforced concrete piers (heights ranging from 20 to 140 m). The experiment aimed to investigate daily deformation patterns of the highest bridge pier (Figure 1, left) with approximate dimensions: 140 m (height) x 15 m (width at west/east side) x 7 m (width at south/north side). For this purpose, the pier was measured from two perpendicular sides using two high-end TLSs (Figure 2): Leica ScanStation P50 and a Zoller+Fröhlich Imager 5016 (ZF5016). The main deformations are expected in the west-east direction (along the bridge).

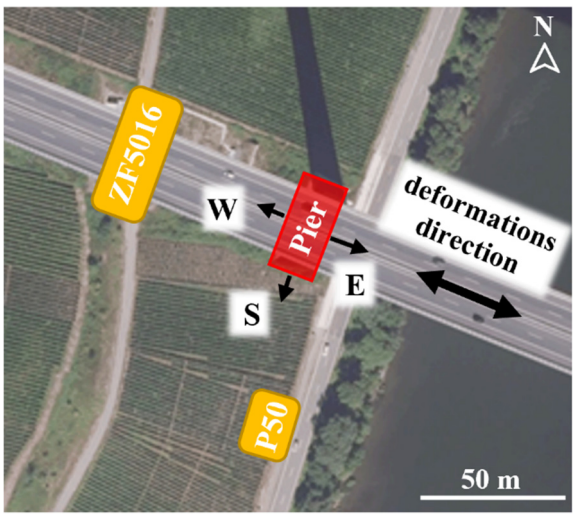


Figure 2. Sketch of the measurement setup (red rectangle - monitored pier, yellow rectangles - scanner positions). Image source: geoportal.de.

For both scanners, the highest scanning resolution (0.8mm@10m) was used with the lowest measurement quality (= no internal point averaging). Furthermore, the in-built dynamic dual axis compensators were used to assure the verticality of the instruments.

The measurements were conducted on 26 August 2020. The temperature changes of 13.4°C to 21.4°C during the day were expected to induce deformations due to thermal expansion in for us detectable range - up to 15 mm of the pier length extension (Brooks, 2014) accompanied with additional unknown shape deformations. However, due to a cloudy sky, which hinders direct and uneven material heating, the deformations were expected to be far from the extreme values. Namely, the bridge bearings are designed for the maximum pier movement of ±550 mm at the highest elevation (Kuschnerus *et al.*, 2021).

The P50 was placed south of the pillar, perpendicular to the expected deformations, reaching measurement distances of 100-180 m. The measurements were taken between 11:37 and 18:02, where 26 epochs were measured with 15 min intervals. The ZF5016 was positioned west of the pillar, in line with the expected movement, being approximately 80 m away. The measurements were taken from 09:53 until 16:24, also with approximately 15 minutes intervals, resulting in 27 epochs.

The changes of atmospheric conditions through the measurement campaign had a systematic impact of up to 1 mm on the measured distances (1 ppm per 1°C), which is within the expected noise level. Hence, no atmospheric corrections were applied. To account for eventual instrument instability over time, which was reported in previous studies (Janßen *et al.,* 2020; Kuschnerus *et al.,* 2021), four dedicated BOTA8 scanning targets (Janßen *et al.,* 2019) were placed on tripods around the scanner stations at distances of approximately 30 m. In the case of ZF5016, the targets were visible within each scan of the object of interest. Hence, all consecutive scans were registered to the local scanner coordinate system of the first scan (epoch 0).

For the point clouds acquired with P50 the same was not possible because: A) the scanner software does not allow simultaneous scanning in the front and the back without selecting a full panoramic scan, which would drastically increase scanning time and; B) it was not possible to place the targets in a way to circumvent the latter problem in the given surrounding. Hence, for efficiency, the targets were measured only at the very beginning and the end of the scanning campaign, to check for the eventual instrument instability. This solution was suboptimal, with an impact on the following analysis (see Section IV). However, it was a necessary compromise between the temporal resolution of consecutive scans and the assurance of instrument stability.

The target centers were estimated using the template matching algorithm described in (Janßen *et al.,* 2019), while the target-based point cloud registration was done in Leica Cyclone, using the in-built functionalities.

### A. *Compared deformation magnitudes*

As the ZF5016 was placed with the line of sight parallel to the direction of the expected pier deformations (Figure 2), its measurements were processed with the established M3C2 algorithm, which provides signed magnitudes as deformation estimates, with the sign depending on the deformation direction relative to the surface normal. These values served as an independent reference for validating the keypoint-based algorithm.

The P50 scans covered two perpendicular pier walls (Figure 2), the south wall with a 2.5° angle of incidence at instrument height and the east wall with an 85° incidence angle. As the line of sight was nearly perpendicular to the expected deformations (west-east direction, along the south wall), its scans were primarily used for testing the keypoint-based algorithm.

To get an additional (but not independent!) validation of the keypoint-based algorithm, the east wall surface was separated from P50 scans and additionally processed with the M3C2 algorithm. Hence, the three estimates of the pier deformation magnitudes were compared and analyzed: M3C2 differences of ZF5016 point clouds (west wall), M3C2 differences of P50 point clouds (east wall) and keypoint-based deformation estimates (Section II) from P50 point clouds (south wall).

The M3C2 deformation magnitude estimates are defined along the normal of the observed pier wall surfaces. As the east wall observed with P50 and the west wall observed with ZF5016 are parallel, both M3C2 deformation estimates can be directly compared. The deformation vectors retrieved with the keypoint-based approach have, however, arbitrary direction in space (Eq. 2). To compare their magnitudes to the M3C2 estimates, we first estimated the mean normal vector of the pier's east wall $\boldsymbol{n}_E$ (from P50 scans), along which M3C2 differences are estimated. Then we projected the vectors estimated with keypoint-based approach ($\overline{\boldsymbol{v}}_i^s$ in Eq. 2) onto this normal vector by (Eq. 5):

$$\overline{\boldsymbol{p}}_i^s = (\overline{\boldsymbol{v}}_i^s \cdot \boldsymbol{n}_E) \times \boldsymbol{n}_E \qquad (5)$$

where $\overline{\boldsymbol{p}}_i^s$ is the projected vector of deformations. To finally get signed deformation magnitudes comparable to M3C2 values, $d_i^s$ are estimated as $d_i^s = \|\overline{\boldsymbol{p}}_i^s\|$ instead of $d_i^s = \|\overline{\boldsymbol{v}}_i^s\|$ (Eq. 4). And each $d_i^s$ was given a positive sign for deformation in the west direction and a negative for the east. This strategy disregards the fact that the normals of the pier's east wall vary by maximally 2° over the whole surface. However, these changes influence the estimated deformation magnitudes by maximally 0.06 % of their value, which is negligible. Moreover, the angle between the Z-axis and normal vector $\boldsymbol{n}_E$ is 89.3°. Hence, all compared deformation magnitudes can be considered as horizontal.

## IV. Results and Discussion

The following section covers the results of the first analysis and the whole process is still a work in progress. Figure 3. presents the estimated signed deformation magnitudes relative to the pier height and time passed from epoch 0 ($dt$ in hours). The data points are presented for every 10 m of the height and every 0.5 h for the passed time $dt$ (lines of different colors). The values of the signed keypoint magnitudes are generated by evaluating the approximation function (Eq. 3), while the M3C2 values are estimated at specified heights and linearly interpolated considering scanning time.

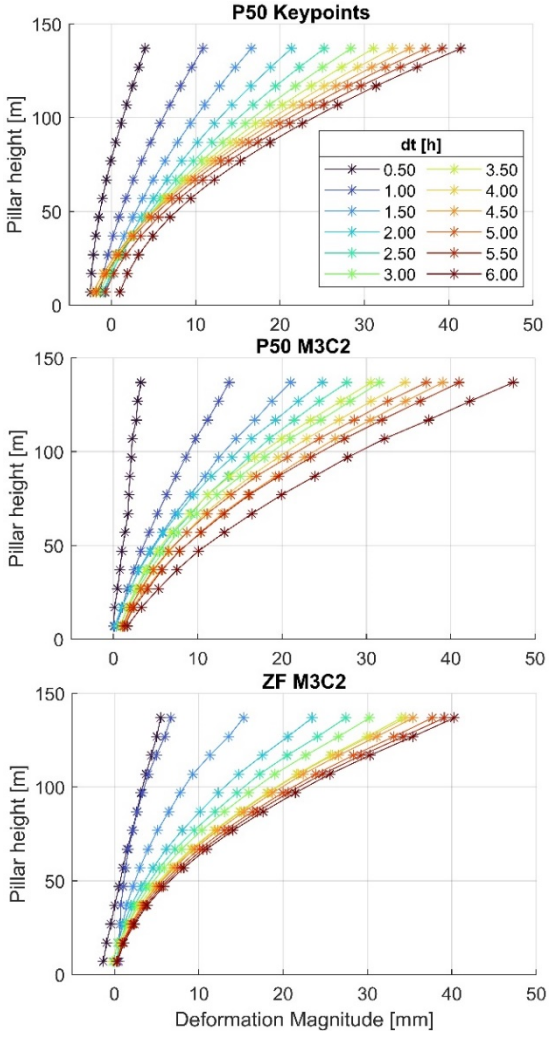


Figure 3. Pier deformation estimates (signed magnitudes) relative to the height and time passed from epoch 0: proposed approach (top) vs. reference values (middle and bottom).

The figure refers to the full scanning time series of both scanners (approx. 6 hours), with only partially overlapping scanning time (3 h overlap), where $dt$ for each scanner refers to the different epoch 0 (ZF5016 09:53, P50 11:37). It serves only for a rough comparison of the algorithms and illustration of the range and form of the pier deformations over an extended period.

It can be observed that the pier exhibited non-linear deformations and bending over time due to temperature-related material expansion (an increase of tilt and curvature with time *dt*), reaching the magnitudes of approximately 40 mm at the pier top after 6 h. The form and range of deformations are directly comparable for the proposed algorithm and M3C2 estimates. The latter holds true, although the scanning times of P50 and ZF5106 are not directly comparable. This is explainable by nearly linear temperature increase during the whole measurement campaign, reaching the highest point of 21.4°C somewhat before 18:00 (see Section II.).

To assure adequate quantitative evaluation of the approaches the following analysis focuses only on the overlapping time window of both scanners (from 13:00 until 16:15, presented in Figure 4). The reference epoch 0 used to define the initial state of the bridge pier is similar, but not perfectly matching between the scanners (12:57 for P50, 12:59 for ZF5016). To achieve a direct comparison, the deformation estimates refer to the same pillar heights and times of the day (evaluating an approximation function for the keypoints and linearly interpolating for M3C2).

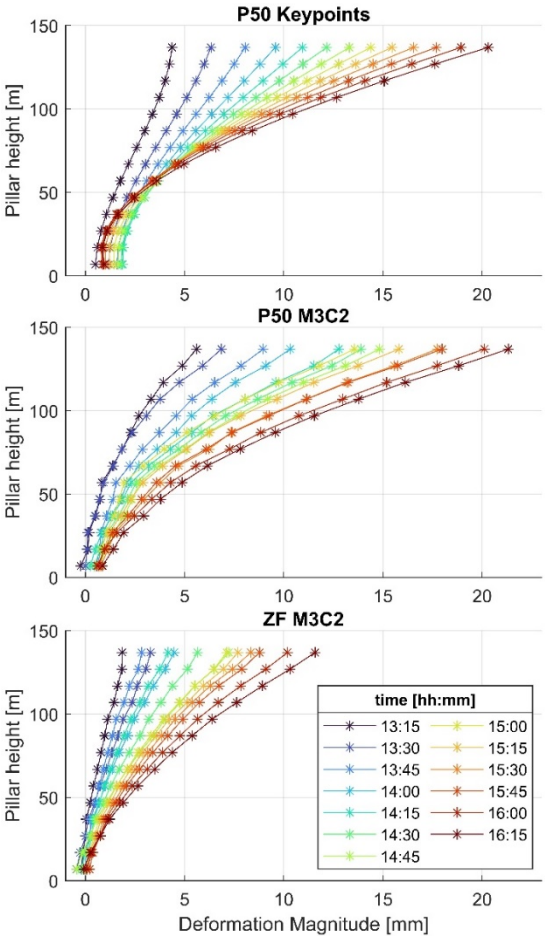


Figure 4. Pier deformation estimates (signed magnitudes) relative to the height and scanning time – focusing on the overlapping scanning times of ZF5016 and P50: proposed approach (top) vs. reference values (middle and bottom)

The mismatches between the estimated deformations of all 3 solutions (*P50 keypoints* vs. *ZF5016 M3C2* and *P50 M3C2*) were calculated as the differences of the corresponding data points in Figure 4. The mean differences between the corresponding data points were 2.4 mm for *ZF5016 M3C2* and 0.4 mm for *P50 M3C2* respectively, while the maximal differences reached almost 10 mm between *P50* and *ZF5016*. These large differences between the keypoint-based solution to the independent reference (*ZF5016 M3C2*) indicates a systematic bias. As the differences between *P50 keypoint-based* and *P50 M3C2-based* estimates are much smaller, it seems that the observed bias is due to the scanner, and not the estimation method. We assume that the source of the error is instrument instability, and we attribute it to the scans of P50 rather than ZF5016 due to the lack of an adequate registration regime for all scans (see Section III).

The standard deviation (std) between the P50 keypoint-based solution and ZF5016 M3C2 was 1.4 mm, and compared to P50 M3C2 was 0.9 mm. These values are within the expected range. Namely, the keypoint based deformation magnitudes $d_i^s$ are estimated from the mean of approx. 40 keypoint matches (average of all segments and epochs), while the std of the coordinate differences $[\Delta X, \Delta Y, \Delta Z]_i^j$ was on average 2.4 mm for $\Delta X$ and $\Delta Y$, and 3.5 mm for $\Delta Z$. This results in a single vector ($\boldsymbol{v}_i^j$) magnitude uncertainty of approx. 5 mm. By using simple variance propagation by the square root of n matches, the expected std of the averaged deformation magnitude is 0.8 mm, falling close to the previously presented values.

Hence, this simple analysis suggests that the uncertainty is primarily influenced by the observed bias, while the precision of the proposed approach is within the expected range of a few millimeters. We argue that the instrument instability is the main limiting factor of the overall accuracy of the proposed approach. Our initial results (based on this case study) suggest that the keypoints detected in the intensity images can be used as natural targets to detect centimeter-level deformations with millimeter-level uncertainty if we take care of the instrument instability. However, further experiments are necessary to support these claims.

In the following sections, two aspects will be addressed, which we perceived as impactful and relevant for future applications of keypoint-based deformation monitoring: A - dealing with the abovementioned instrument instability, and B - specific adaptations and possible improvements of the implemented algorithm.

### A. *Instrument instability*

To reach comparable deformations between ZF5016 and P50 data (Figure 3 and 4) it was necessary to account for instrument instabilities that can occur during long-term TLS observations (Janßen *et al.,* 2020; Kuschnerus *et al.,* 2021). In the case of the reference

dataset acquired by the ZF5016 scanner, this was done by accurate target-based registration (Section III).

In the case of P50 scans, such an approach was not possible (Section III). Instead, we used the presumption that the temperature-related material expansion during our measurements could not have caused the larger displacements of the pier just several meters above its 47 m deep and 20 m wide fundament (Schmidt-Hurtienne and Krumbein, 2019). The presumption is supported by the observation that the maximal M3C2 differences with ZF5016 were less than 2mm at the pier bottom (Figure 3). However, definite proof of validity is missing. We numerically implemented this presumption by subtracting the deformation magnitudes estimated with M3C2 for the lowest pier segment from all segments within each point cloud acquired by P50.

The M3C2 deformation estimates from P50 data initially indicated a slow movement (drift) of the bridge pier base reaching maximally 7.6 mm for the 8th scan in series (Figure 5, corresponds approximately to $dt$ of 1.0 h in Figure 3). Such behavior is unexpected, and it was not observed in the independent ZF5016 dataset. Additional investigation, using two BOTA8 laser-scanning targets that were included in each of 26 P50 scans, showed that this drift can be attributed to the scanner instability. Tracing the target center coordinate changes of two targets showed nearly identical drifting patterns over time (Figure 5), which can be explained by the scanner turning around its standing axis.

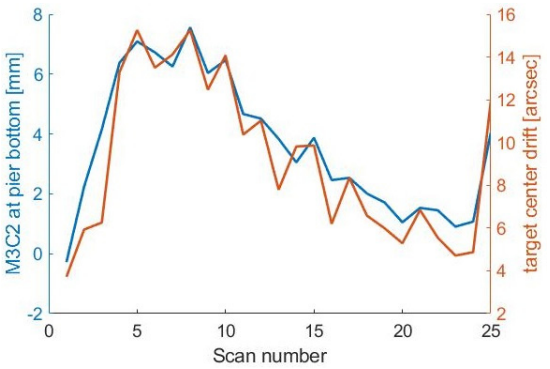


Figure 5. Drift of P50 M3C2 deformation magnitudes at lowest segment of the bridge pier vs. drift of the BOTA8 target coordinates (polar coordinate – horizontal angle, average of 2 targets).

Within this work, we successfully mitigated some of the systematic bias due to scanner instability by leveraging prior presumption about the measurement object. Such a solution cannot be generalized and depending on the error source and its impact on the measurements it could be even impossible to separate it from the observed deformations. The non-zero mean differences between keypoint-based and M3C2 solutions (particularly with ZF5016 data) point out that some systematic errors (*e.g.*, scanner tilting perpendicular to the line of sight or instability of collimation and trunnion axis errors) are remaining in our data and that they are limiting the achievable sensitivity and accuracy of the TLS based deformation monitoring.

The strategy we applied here can remove the impact of translational errors and the rotation around the instrument's standing axis. However, other systematic influences could have impacted our measurements in such a way that this bias would be nearly perfectly correlated with the observed deformation pattern. Such systematic influences are for example: tilting of the instrument, changes in dynamic compensator zero value, and changes of the instrument's internal systematic errors (*e.g.* trunnion or collimation axis error). All three effects can be induced by changes in the ambient and internal instrument temperature (Medić *et al.,* 2020; Janßen *et al.,* 2020).

The abovementioned influences can have an impact both on M3C2 differences and the keypoint-based deformation estimates. However, the majority of the known systematic effects impact the coordinates in the direction perpendicular to the line of sight and minor parts along the line of sight. Hence, the keypoint-based deformation estimates are generally more sensitive, as M3C2 differences are commonly estimated approximately along lines of sight. In this particular study, the latter applies for M3C2 differences of ZF5016, but not of P50, as the observed pier surface with P50 has nearly perpendicular normal to the line of sight (observed with a high incidence angle of 85°). Hence, both keypoint-based and M3C2 deformation estimates with P50 are similarly systematically influenced, causing their good correspondence (better than with ZF5016 data).

The conducted deformation monitoring experiment again highlights that great care should be placed in adequate registration and calibration of TLS point clouds to reach sufficient measurement accuracy for demanding deformation monitoring tasks.

### B. *Aspects of the implemented algorithm*

The implemented algorithm can be simply adapted for a more general case of deformation monitoring. First, the current implementation models deformations as a function of time, which can be adapted to any quantity of interest (*e.g.*, force or temperature). Second, introducing the local rigidity presumption and splitting the field of view into segments for outlier removal and averaging needs to be adapted according to the dimensions and expected behavior of the monitored object. Third, the functional approximation of the deformation behavior needs to be adapted to specific use cases.

The implemented algorithm can be further improved in several ways: parameter tuning; testing different feature detectors, descriptors, and their combinations; considering different solutions for the functional approximation of keypoint-based deformation estimates; as well as including automated point cloud

registration and in-situ calibration routines within the workflow. Furthermore, the algorithm is currently limited to scanning with a single instrument from a single scanner station. This could be extended to multiple stations at different locations and with different instruments, if the scanner intensity values could be radiometrically calibrated to achieve good correspondence between the scans. Also, any change in relative geometry between scanner station and scanned object introduces distortions of the intensity and range images which should be correctly modeled and removed. Lastly, the current algorithm implementation searches for keypoint correspondences only between epoch 0 and epoch i. This could be extended to searching corresponding keypoints between all combinations of scans increasing the number of observations and, hence the precision of deformation estimates.

The factors influencing the sensitivity of the implemented approach should be further investigated. Primarily this refers to the properties of the particular scanner and scanning settings. For example, the role of the footprint size and scanning resolution on the quantity and quality of the detected keypoints is unclear.

Finally, the proposed algorithm can be used as a stand-alone alternative to existing monitoring approaches, targeting certain monitoring tasks. However, there is an unexploited potential in combining it with other complementary existing TLS-based deformation analysis methods to increase sensitivity in certain directions. For example, combining it with M3C2 would assure sensitivity both in the directions parallel and perpendicular to the surface normal. Alternatively, the point clouds could be screened for regions with different geometric and radiometric properties and the choice of the deformation analysis method could be automatically adapted accordingly.

## V. Conclusion

In this work, we demonstrated a new 2D keypoint-based deformation monitoring algorithm for deformation monitoring with terrestrial laser scanners from a single scanner station. The algorithm relies on representing the series of TLS point clouds as spherical intensity and range images and using established 2D image feature detection and description algorithms. The approach was tested in a case study of monitoring daily deformations of a bridge pier due to temperature-related material expansion.

The achieved results show that the proposed method can be used to detect cm-level deformations with an uncertainty of several millimeters, even along the surface of the object of interest. This complements the established approaches for deformation monitoring with TLS point clouds, as they are mostly insensitive to deformations occurring laterally over the measured surface. This is especially true in the case of structural health monitoring, where measured objects often lack sufficiently indented surface structures.

The analysis of the results indicated that the presence of systematic biases due to TLS instability is one of the main factors limiting the achievable accuracy. Hence, integrating adequate point cloud registration and TLS calibration routines is necessary to increase the achievable sensitivity of TLS-based deformation monitoring. Finally, we discussed in detail how the implemented algorithm can be further improved. Our future efforts will primarily focus on adapting the algorithm for a general case of TLS-based deformation monitoring.

## VI. Acknowledgements

Dido Monzel and Martin Blome have acquired the dataset.

## References

Bay, H., A. Ess, T. Tuytelaars, and L. V. Gool (2008). Speeded-up Robust Features (SURF). *Computer Vision and Image Understanding* 110 (3): 346–59.

Brooks, J. (2014). Concrete and masonry movements. Butterworth-Heinemann, pp. 459-460.

Friedli, E., and A. Wieser (2016). Identification of Stable Surfaces within Point Clouds for Areal Deformation Monitoring. In *Proceedings of the 3rd Joint International Symposium on Deformation Monitoring (JISDM). Vienna, Austria. 30th March-1st April*.

Gojcic, Z., L., Schmid, and A. Wieser (2021). Dense 3D displacement vector fields for point cloud-based landslide monitoring. *Landslides* 18: 3821–3832.

Gojcic, Z., C. Zhou, and A. Wieser (2020). F2S3: Robustified determination of 3D displacement vector fields using deep learning. *Journal of Applied Geodesy* 14(2): 177–189

Holst, C., J. Janßen, B. Schmitz, M. Blome, M. Dercks, A. Schoch-Baumann, J. Blöthe, L. Schrott, H. Kuhlmann, and T. Medic (2021). Increasing Spatio-Temporal Resolution for Monitoring Alpine Solifluction Using Terrestrial Laser Scanners and 3d Vector Fields. *Remote Sensing* 13 (6).

Holst, C., L. Klingbeil, F. Esser, and H. Kuhlmann (2017). Using Point Cloud Comparisons for Revealing Deformations of Natural and Artificial Objects. In *Proceedings of the 7th International Conference on Engineering Surveying (INGEO 2017), Lisbon, Portugal*, pp. 18-20.

Janßen, J., H. Kuhlmann, and C. Holst. (2020). Assessing the Temporal Stability of Terrestrial Laser Scanners during Long-Term Measurements. In *Contributions to International Conferences on Engineering Surveying, INGEO & SIG 2020*. Dubrovnik, Croatia.

Janßen, J., T. Medić, H. Kuhlmann, and C. Holst (2019). Decreasing the Uncertainty of the Target Centre Estimation at Terrestrial Laser Scanning by Choosing the Best Algorithm and by Improving the Target Design. *Remote Sensing* 11 (7) (7).

Jing, J., T., Gao, W., Zhang, Y., Gao, and C., Sun (2021). Image Feature Information Extraction for Interest Point Detection: A Comprehensive Review. *ArXiv Preprint* ArXiv:2106.07929.

Lague, D., N. Brodu, and J. Leroux (2013). Accurate 3D Comparison of Complex Topography with Terrestrial Laser Scanner: Application to the Rangitikei Canyon (NZ). *ISPRS Journal of Photogrammetry and Remote Sensing* 82, pp. 10–26.

Leutenegger, S., C. Margarita, and Y. S. Roland (2011). BRISK: Binary Robust Invariant Scalable Keypoints. In *2011 International conference on computer vision, pp. 2548-255.*

Kuschnerus, M., D. Schröder and R. Lindenbergh (2021). Environmental influences on the stability of a permanently installed laser scanner. In: *Int. Arch. Photogramm. Remote Sens. Spat. Inf. Sci. - ISPRS Arch.*, 43, pp. 745–752.

Medić, T., H. Kuhlmann, and C. Holst (2019). Automatic In-Situ Self-Calibration of a Panoramic TLS from a Single Station Using 2D Keypoints. In *ISPRS Ann. Photogramm. Remote Sens. Spat. Inf. Sci*.

Medić, T., H. Kuhlmann, and C. Holst (2020). A Priori versus In-Situ Terrestrial Laser Scanner Calibration in the Context of the Instability of Calibration Parameters. In *Contributions to International Conferences on Engineering Surveying, INGEO & SIG 2020*, Dubrovnik, Croatia.

Mukupa, W., G. W. Roberts, C. M. Hancock, and K. Al-Manasir (2017). A Review of the Use of Terrestrial Laser Scanning Application for Change Detection and Deformation Monitoring of Structures. *Survey Review* 49 (353), pp. 99–116.

Neuner, H., C. Holst, and H. Kuhlmann (2016). Overview on Current Modelling Strategies of Point Clouds for Deformation Analysis. *Allgemeine Vermessungs-Nachrichten (AVN)* 123 (11–12), pp. 328–39.

Schmidt-Hurtienne, B. and O. Krumbein (2019). Gründung und Unterbauten der Hochmoselbrücke – Planung und Ausführung. *Bautechnik*, 96, pp. 21–30.

Szeliski, R. (2022). Feature detection and matching. In *Computer Vision*. Springer, pp. 333–399.

Urban, S., and M. Weinmann (2015). Finding a Good Feature Detector-Descriptor Combination for the 2D Keypoint-Based Registration of TLS Point Clouds. In *ISPRS Ann. Photogramm. Remote Sens. Spat. Inf. Sci., ISPRS Geospatial Week 2015*, II-3/W5, pp. 121–28.

Wagner, A., W. Wiedemann, and T. Wunderlich (2017). Fusion of Laser Scan and Image Data for Deformation Monitoring – Concept and Perspective. In *Proceedings of the 7th International Conference on Engineering Surveying (INGEO 2017)*, pp. 157-164.

Wujanz, D., D. Krueger, and F. Neitzel (2016). Identification of Stable Areas in Unreferenced Laser Scans for Deformation Measurement. *Photogrammetric Record* 31 (155):, pp. 261–80.